Variant selection in laser powder bed fusion of non-spherical Ti-6Al-4V powder

Mohammadreza Asherloo ^a, Ziheng Wu ^b, Julian E.C. Sabisch ^c, Iman Ghamarian ^d, Anthony D. Rollett ^e, *, Amir Mostafaei ^a, *

Abstract

The presence of α/α' on prior β/β grain boundaries directly impacts the final mechanical properties of the titanium alloys. The β/β grain boundary variant selection of titanium alloys has been assumed to be unlikely owing to the high cooling rate in laser powder bed fusion (L-PBF). However, we hypothesize that powder characteristics such as morphology (non-spherical) and particle size (50-120 µm) could affect the initial variant selection in L-PBF processed Ti-6Al-4V alloy by locally altering the cooling rates. Despite the high cooling rate found in L-PBF, results showed the presence of β/β grain boundary α' lath growth inside two adjacent prior β grains. Electron backscatter diffraction micrographs confirmed the presence of β/β grain boundary variant selection, and synchrotron X-ray high-speed imaging observation revealed the role of the "shadowing effect" on the locally decreased cooling rate because of keyhole depth reduction and the consequent β/β grain boundary α' lath growth. The self-accommodation mechanism was the main variant selection driving force, and the most abundant α/α boundary variant was type 4 $(63.26^{\circ})/[\overline{10}\ 5\ 5\ \overline{3}]$). The dominance of Category II α lath clusters associated with the type 4 α/α boundary variant was validated using the phenomenological theory of martensite transformations and analytical calculations, from which the stress needed for the $\beta \rightarrow \alpha'$ transformation was calculated.

Keywords: Variant selection; Phase formation; Additive Manufacturing; Hydride-dehydride powder; Texture analysis; Electron backscattered diffraction.

^a Department of Mechanical, Materials and Aerospace Engineering, Illinois Institute of Technology, 10 W 32nd Street, Chicago, IL 60616, USA

^b Materials Engineering Division, Lawrence Livermore National Laboratory, 7000 East Ave, Livermore, CA 94550, USA

^c Samuel Roberts Noble Microscopy Laboratory, University of Oklahoma, Norman, OK 73019, USA

^d School of Aerospace and Mechanical Engineering, University of Oklahoma, Norman, OK 73019, USA

^e Department of Materials Science and Engineering, Carnegie Mellon University, Pittsburgh, PA 15213, USA

^{*} Corresponding authors: A.D. Rollett (rollett@andrew.cmu.edu) and A. Mostafaei (mostafaei@iit.edu)

1. Introduction

Fusion-based additive manufacturing (AM) of titanium alloys such as laser powder bed fusion (L-PBF) or electron beam powder bed fusion (EB-PBF) is known to create a columnar prior β grain structure parallel to the build direction (BD), which appears equiaxed in a horizontal cross-section. Along with strong prior β grain solidification texture with <100>//BD, the subsequent α phase textures are formed via the Burgers orientation relationship (BOR) that is characteristic of the body-centered cubic (bcc) to hexagonal close-packed (hcp) transformation [1–3]. The BOR defines twelve α phase variants that can be formed with respect to the prior β grain orientation [4]. Bias in the relative frequency of the twelve variants is known as variant selection [5,6]. Variant selection results in an α phase texture in AM parts that differs from what might be expected from the typical <100>//BD in the prior β grains, which affects the anisotropy in mechanical behavior of AM parts [7]. Note that a strong influence on the BCC to HCP transformation is the minimization of shape strain caused by the extremely high cooling rates in the L-PBF process [8,9].

Variant selection is governed by three possible mechanisms of (1) certain β/β grain boundary characteristics at elevated temperatures, i.e., \approx 900 °C, that favor the nucleation of specific α variants during the solid-state phase transformation in the cooling process [10–12], (2) nucleation and growth of three different variants with a shared <11 $\bar{2}$ 0> direction in a cluster known as the self-accommodation process in order to minimize the transformation strain [13–17], and (3) presence of metastable α particles above β transus temperature that acts as preferred nucleation sites for particular α variants during the cooling process [5,18]. The grain boundary variant selection results in either (i) an α grain holding the special BOR with both adjacent prior β grains or (ii) an α grain sharing a basal plane with the α grain on the opposite side of the β/β boundary. Regardless of the type of α phase produced from β grain boundary variant selection, the α grains on both sides of the so-called β/β boundary have crystallographically similar orientations, thus, they reduce the barriers to dislocation movement during the deformation [19]. The variant selection process can intensify the texture and increase the anisotropy of the mechanical properties of Ti-6Al-4V [20–22].

There have been various studies on variant selection in AM fabricated Ti-6Al-4V. DeMott et al. [23] used 3D electron backscatter diffraction (EBSD) to study the variant selection phenomena

in EB-PBF processed parts and demonstrated the presence of three-grain clusters of α variants. Stephenson *et al.* [24] investigated the effect of scanning strategy on variant selection in EB-PBF parts. They demonstrated such that a linear scan pattern, i.e., no rotation resulted in self-accommodation dominance and a random scan resulted in β grain boundary variant selection. Lu *et al.* [7] reported that hot isostatic pressing (HIP) intensified the texture of the Ti-6Al-4V parts produced by the EB-PBF process because of α variant selection and subsequent reduction in the deformation constraints of the parts. Simonelli *et al.* [25] studied α variant selection during L-PBF with spherical Ti-6Al-4V powder and concluded that the high cooling rate minimized the chance of β grain boundary variant selection. The α' martensite texture was correspondingly random with a high density of small α' grains inside each prior β grain. Kamath *et al.* [26] studied the effect of spot-melt scanning strategy on the variant selection during EB-PBF of Ti-6Al-4V powder compared to the linear scan strategy. They reported that the texture intensity gradually increased with build height with 0° scanning, however, the spot-melt strategy did not show this trend. Moreover, they showed that the variant selection was more distinct when the spot-melt strategy was used compared to the linear strategy.

To broaden feedstock in powder bed AM processes, use of non-spherical powder can significantly lower the powder production cost [27–29]. Moreover, powder size metrics and morphology can alter PBF process parameters thus optimization is required to attain a relative density of 99.8 % [30,31] while minimizing defect density (i.e., pores and surface roughness) [32], and obtain mechanical properties comparable to parts manufactured with spherical powder [33–36]. Variant selection in AM parts fabricated using spherical powders has been extensively studied, however, the effect of using non-spherical powder has not been investigated. In this study, however, non-spherical powder with size distribution of 50-120 μ m was used to understand the effects of morphology/size combination on the texture evolution and α variant selection during L-PBF with Ti-6Al-4V alloy. This is important because variant selection and texture evolution directly affect the final properties of the AM parts. First, the occurrence of variant selection is demonstrated, then, the significance of each α variant selection mechanism is discussed during the thermal cycles through the β transus associated with the L-PBF process.

2. Materials and methods

Non-spherical hydride-dehydride (HDH) Ti-6Al-4V powder (see Figure 1a) was supplied by Kymera International – Reading Alloys with the powder size distribution (PSD) of $50-120~\mu m$ and chemical composition given in

Table 1. The PSD was also analyzed using LS13 320 XR System: $d_{10} = 54.66 \mu m$, $d_{50} = 85.1 \mu m$, $d_{90} = 119.4 \mu m$, with a mean size of 84.8 μm , and average circularity of 0.68 (see Figure 1b). Note that only 6 % of powder particles were smaller than 40 μm , and all measurements reported as spherical equivalent diameter of the powder particles. Powder morphology was confirmed by scanning electron microscopy (SEM, model JEOL 5900LV), as shown in Figure 1a.

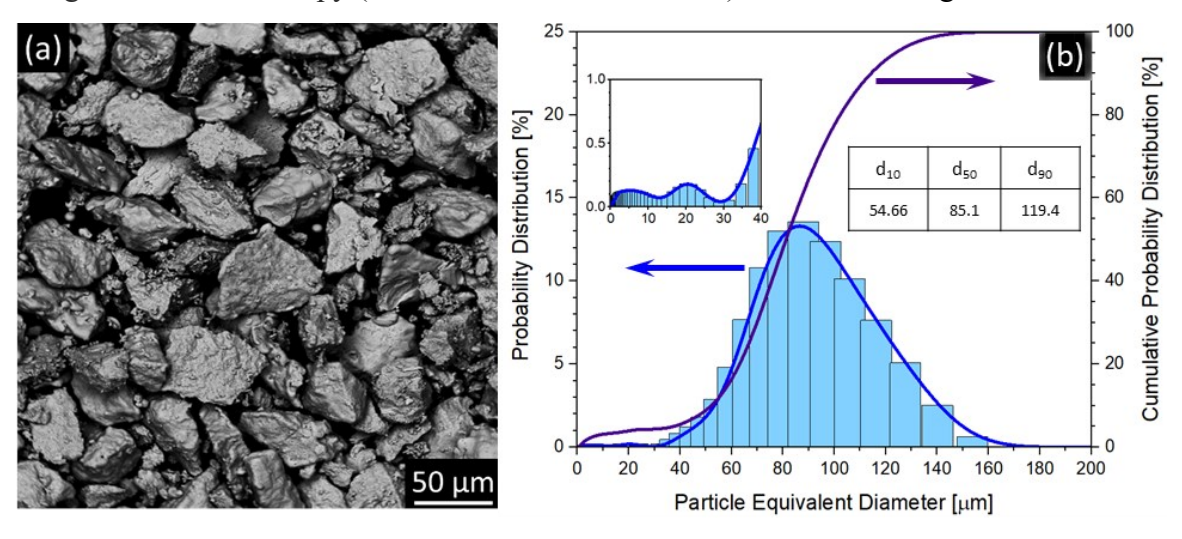


Figure 1. (a) Scanning electron micrograph and (b) particle size distribution of non-spherical Ti-6Al-4V powder. The inset plot in (b) shows the powder particle size probability distribution for particles smaller than 40 µm.

Table 1. Chemical composition of non-spherical Ti-6Al-4V powder provided by the manufacturer compared to the nominal composition per ASTM B 348 standard [2]. Units for all values are wt.%.

	Ti	Al	V	Fe	С	Н	N	O
Nominal composition (wt. %)	Bal.	5.5-6.75	3.5-4.5	< 0.40	< 0.08	< 0.015	< 0.05	< 0.20
non-spherical powder	Bal.	6.08	3.88	0.19	0.02	0.005	0.02	0.17

Coupons with dimensions of $15 \times 10 \times 10 \text{ mm}^3$ were L-PBF processed in an EOS 290M machine. Laser power of 370 W, laser scan speed of 1250 mm/s, hatch spacing of 90 μ m, and layer thickness of 60 μ m were used as the optimized processing parameters (which results in part with a relative density of > 99.8%), described in Ref. [31]. Coupons were cut off from the base plate using a wire electrical discharge machining (wire-EDM, model GF Machining Solutions AC Progress VP3).

Samples were cross-sectioned parallel to the build direction using a Mitsubishi FX10k wire-EDM Machine. Slices were hot-mounted using phenolic thermosetting powders (MetLab) and a compression molding process for metallographic observations. Afterward, samples were ground up to 800 grit size sandpapers, polished using 1 μm and 0.05 μm alumina solutions, followed by a final polishing using 0.04 μm colloidal silica. To observe microstructure and texture, an SEM microscope (JEOL 5900LV) equipped with an electron backscatter diffraction (EBSD, Oxford Instruments) was used at an accelerating voltage of 20 keV and step size of 0.5 μm. Data was collected using AzTec software from the center of cross-sections and analyzed using the HKL Channel 5 software package. Also, a open source MATLAB-based toolbox called "MTEX" [37] was used to reconstruct the prior β grains (PBG), extract the crystallographic orientation distributions, measure the crystallographic textures, and study the variant selection and orientation relationship (OR) based on the EBSD results. All the prior β/β grain boundaries with the misorientation angle < 10° were analyzed for grain boundary α ′ growth based on Ref. [25,38].

The L-PBF processed non-spherical Ti-6Al-4V powder was sectioned using a Southbay Technology Model 650 low-speed diamond wheel saw. One section was then ground to 150 μ m thickness using progressively coarser grits up to 1000 grit SiC sandpaper. The sample was cut into 3 mm disks and dimple ground using a Fischione model 200 dimpling grinder with 6 μ m diamond, 3 μ m diamond, 1 μ m diamond, and finally 0.02 μ m SiO₂ to a thickness of 10 μ m. The sample was then ion milled in a Gatan Model 600DIF at 4 kV until electron transparent. Then, scanning precession electron diffraction (SPED) was conducted using a 200 keV JEOL ARM transmission electron microscope (TEM). The electron beam was precessed by the NanoMEGAS DigiSTAR unit at the angle of 0.4° with a frequency of 100 Hz and one precession per frame. An area of 2 μ m × 2 μ m was scanned with the step size of 5 nm. The spot diffraction patterns were recorded using a standard Stingray camera. The collected patterns were indexed by cross-correlating them with the quasi-kinematically simulated diffraction patterns made in the automated crystal orientation mapping (ACOM) software for the α' and β titanium crystal structures.

3. Results and discussion

3.1. General microstructural features

The typical microstructure of the L-PBF processed non-spherical Ti-6Al-4V powder consists of acicular α' martensitic phase because of the high cooling rates associated with the AM process (see Figure 2). The optical micrograph showed the general columnar grain structure, the low magnification SEM micrograph showed the different types of α' laths with a 90° angle of growth,

and the high magnification SEM micrograph demonstrated the nano-size β phase particles due to the continuous heat cycles during the L-PBF process which was in agreement with Ref. [39–41].

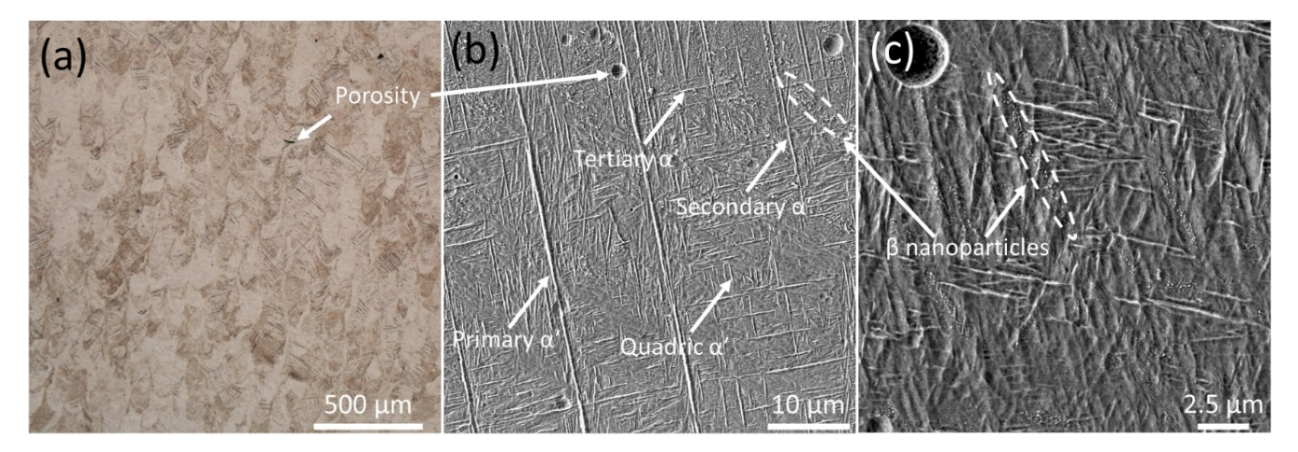


Figure 2. (a) optical micrograph and (b) low and (c) high magnification SEM images of the L-PBF processed non-spherical Ti-6Al-4V powder.

Another important aspect of microstructural features in titanium alloys is the size of α phase laths which has a direct impact on the mechanical properties of the parts. To study the constituent phases and α' lath sizes with more precision, TEM data was collected from the L-PBF processed non-spherical Ti-6Al-4V powder, and the results are shown in Figure 3. Due to the potential overlap between fine α' lath along the TEM foil thickness, a mixture of more than one diffraction pattern usually forms. The multi-indexing algorithm in the ACOM software was used to determine the orientations of fine α' laths that overlap over the TEM foil thickness. In this algorithm, a recorded diffraction pattern is initially indexed to find the most matched simulated pattern (or template), as shown in Figure 3b. Subsequently, the best solution template is subtracted from the recorded diffraction pattern and is re-indexed by detecting the remaining spot diffraction patterns (see Figure 3c). Mapping the pixel-by-pixel changes in the diffraction signal can highlight throughthickness structural features that may otherwise be obscured. The correlation coefficient was used to measure the degree of similarity between the intensities of neighboring diffraction patterns. Very fine α' lath microstructures presented in Figure 3d reveal a considerably large cooling rate during the first cycle of cooling and solidification. These α' laths may grow during successive iterations of heating and cooling and form a wide range of α' lath thickness. Therefore, a broad design space exists to engineer the distribution of α' lath size and significantly improve the strength-ductility balance.

A negligible amount of β phase was detected only in areas of low phase reliability. As shown by an arrow in Figure 3(e,f), some of the detected beta phase regions are located at the interface of α' laths. Since the generated diffraction patterns in these regions are usually a mixture of more than one microstructure/phase, it is challenging to index the acquired diffraction pattern reliably. Therefore, it can be concluded that no β phase exists or the size of the β phase is extremely fine, which is lower than the capability of the SPED technique to detect.

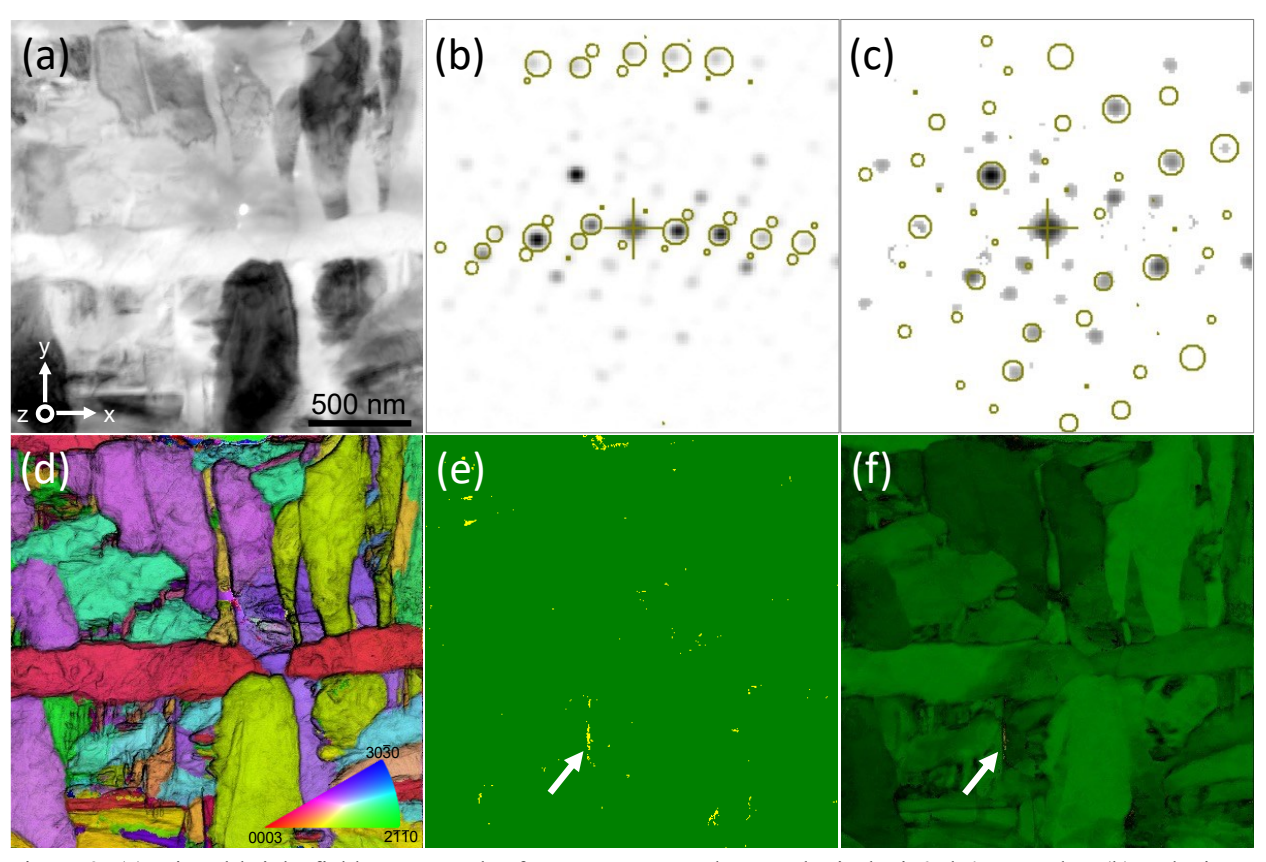


Figure 3. (a) Virtual bright field TEM result of L-PBF processed non-spherical Ti-6Al-4V powder. (b) Indexing a recorded spot diffraction pattern and (c) re-indexing the acquired pattern after removing the diffraction spots detected in (b). (d) plane view of the SPED orientation distribution map overlaid with the correlation coefficient map of the part, note that the overlaid map shows small alpha laths obscured by larger overlapping grains. (e) Phase map and (f) phase map overlaid on the phase reliability map. Note that the reliability of a phase is determined by comparing the index values of the two best-matched diffraction templates.

3.2. Texture analysis

The diffusionless transformation of β to α' during the rapid cooling of the melt pool follows the Burgers Orientation Relationship (BOR) [1]. Burgers showed that twelve α/β variants are expected based on the orientation relationship between the BCC and HCP crystal structures. The (close-packed) basal plane of the HCP {0001} aligns with one of the {110} close-packed planes

in the BCC, and the close-packed direction of the HCP <11 $\overline{2}$ 0> aligns with one of the <111> close-packed directions in the BCC. Combining any two of the twelve variants results in an α/α grain boundary inside a prior β grain. The twelve variants of the BOR are summarized in Table 2.

Table 2. The twelve variants of the Burgers Orientation Relationship (BOR) found in the solid state $\beta \rightarrow \alpha$ transformation.

Variant	Orientation relationship
A	$(1\overline{1}0)_{\beta} \ (0001)_{\alpha} - [111]_{\beta} \ [11\overline{2}0]_{\alpha}$
В	$(10\overline{1})_{\beta} \ (0001)_{\alpha} - [111]_{\beta} \ [11\overline{2}0]_{\alpha}$
C	$(01\overline{1})_{\beta} \ (0001)_{\alpha} - [111]_{\beta} \ [11\overline{2}0]_{\alpha}$
D	$(110)_{\beta} \ (0001)_{\alpha} - [\overline{1}11]_{\beta} \ [11\overline{2}0]_{\alpha}$
Е	$(101)_{\beta} \ (0001)_{\alpha} - [\overline{1}11]_{\beta} \ [11\overline{2}0]_{\alpha}$
F	$(01\overline{1})_{\beta} \ (0001)_{\alpha} - [\overline{1}11]_{\beta} \ [11\overline{2}0]_{\alpha}$
G	$(110)_{\beta} \ (0001)_{\alpha} - [1\overline{1}1]_{\beta} \ [11\overline{2}0]_{\alpha}$
Н	$(10\overline{1})_{\beta} \ (0001)_{\alpha} - [1\overline{1}1]_{\beta} \ [11\overline{2}0]_{\alpha}$
I	$(011)_{\beta} \ (0001)_{\alpha} - [1\overline{1}1]_{\beta} \ [11\overline{2}0]_{\alpha}$
J	$(1\overline{1}0)_{\beta} \ (0001)_{\alpha} - [11\overline{1}]_{\beta} \ [11\overline{2}0]_{\alpha}$
K	$(101)_{\beta} \ (0001)_{\alpha} - [11\overline{1}]_{\beta} \ [11\overline{2}0]_{\alpha}$
L	$(011)_{\beta} \ (0001)_{\alpha} - [11\overline{1}]_{\beta} \ [11\overline{2}0]_{\alpha}$

Wang et al. [42] proposed that six unique types of α/α boundaries can form based on 144 combinations of the BOR between BCC and HCP, as follows:

```
\circ Type 2: 60° // [1 1 \bar{2} 0]
```

o Type 3: 60.83° // [\overline{1.377} \overline{1} 2.377 0.359]

 \circ Type 4: 63.26° // [$\overline{10}$ 5 5 $\overline{3}$]

o Type 5: 90° // [1 \overline{2.38} 1.38 0]

o Type 6: 10.53° // [0 0 0 1]

Type 1 corresponds to two identical or similar α lath orientations resulting in a low angle grain boundary; these were not analyzed quantitatively in this study. However, Types 2 to 6 result in a high-angle grain boundary and are discussed in detail.

EBSD data was collected from horizontal and vertical cross-sections of the L-PBF processed non-spherical Ti-6Al-4V part, and the results are shown in Figure 4. The columnar (vertical cross-sections) and equiaxed (horizontal) grain structures were confirmed by EBSD IPF-Z maps from the color similarity in each prior β grain along with occasional grain boundary alpha, and the results are shown in Figure 4(a₁,b₁). Misorientations between adjacent α' laths were measured from the EBSD data for both cross-sections, and results were shown in Figure 4(a₂,b₂) in the form of a relative frequency distribution. Note that the horizontal cross-section with equiaxed prior β grains

showed the misorientation distribution as the vertical cross-section with columnar prior β grains within statistical variation. The misorientation data showed four main peaks at (1) ~10° associated with type 6, (2) ~60° associated with types 2 and 3, (3) ~63° associated with type 4, and (4) ~90° associated with type 5 α/α boundary variants. By considering randomly generated distributions of α/α boundary types between variants (i.e., in the absence of variant selection), the relative frequency for each type is 9.1 % for type 6, 18.2 % for types 2, 4, and 5, and 36.4 % for type 3, based on their respective contribution to the general 144 combinations of α/β orientation relationship variants. However, as reported by Stanford and Bate [38], the variants of α/α boundaries are not equally distributed, which meant the percentage of each type deviated from the random values. This difference is called "variant selection," in which the frequency of occurrence of each type of variant is non-random, i.e., biased [43].

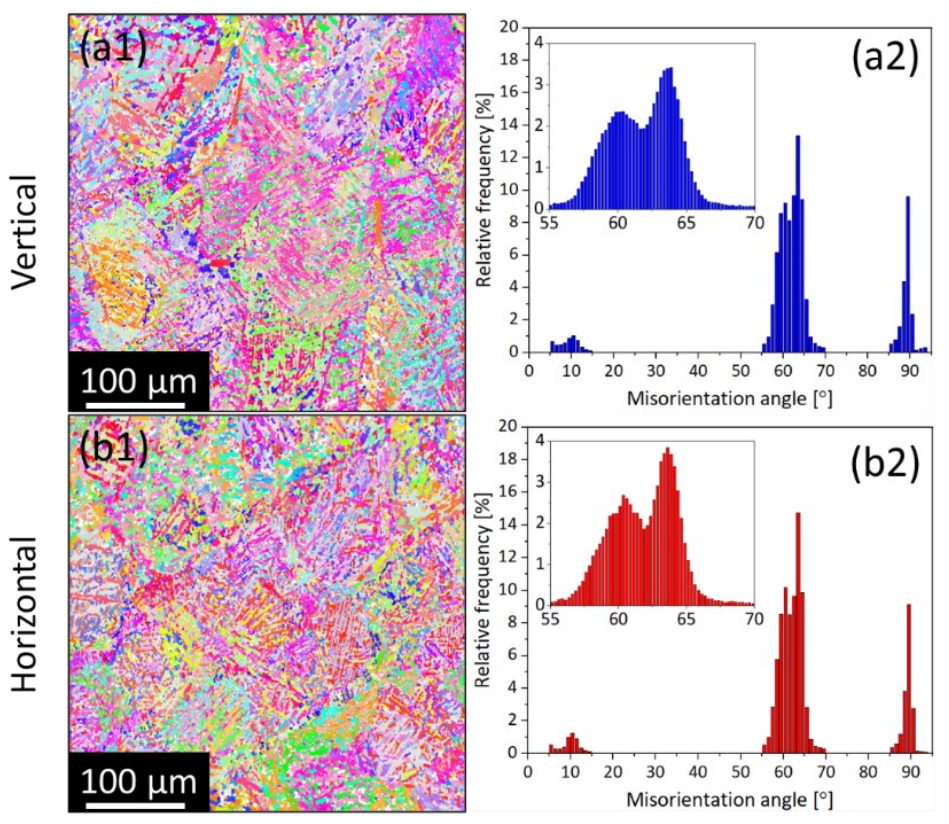


Figure 4. (a1,b1) EBSD IPF-Z maps of the L-PBF processed non-spherical Ti-6Al-4V powder and (a2,b2) misorientation distributions of neighboring α' laths (the inset figures show the misorientation distribution in the range 55-70°).

One way to show the occurrence of variant selection is by showing that the distribution of α' laths orientations for a given prior β grain is biased. To show this, one must reconstruct the prior β grain orientation from the data in the EBSD maps shown in Figure 5. The pole figures of the

selected grains show the orientation distribution of the α' laths inside the selected grains from both cross-sections, along with the superimposed $\{110\}$ poles of each prior β grain shown as black dots. In the absence of variant selection, the α' lath orientations would be uniformly distributed, and the intensities of the poles would be the same. However, the max-to-min ratios of pole densities were 5.0 (vertical cross-section with columnar grains) and 2.1 (horizontal cross-section with equiaxed grains), which differ strongly from unity. Lu et al. [44] reported differences between the variant bias for the equiaxed grains (with a max-to-min ration of 4.6) and columnar grains (with a maxto-min ration of 2.4) in laser directed energy deposition (L-DED) of Ti-6Al-4V. The contradiction in reported pole density ratios in Ref. [44] and the current study could be related to the nature of the equiaxed and columnar grain formations, in which the former was produced by utilizing highintensity ultrasound during the L-DED process. In this study, the equiaxed grains were created due to the scanning pattern in the horizontal cross-section. Note that there have been studies showing fine grain structures near the base plate that turn into strong textures moving away from the build [45], however, in the current study, the EBSD data was collected far from the base plate (~5 mm away from the base plate) to ensure that the potential fine grain structure near the base plate does not affect the overall analysis.

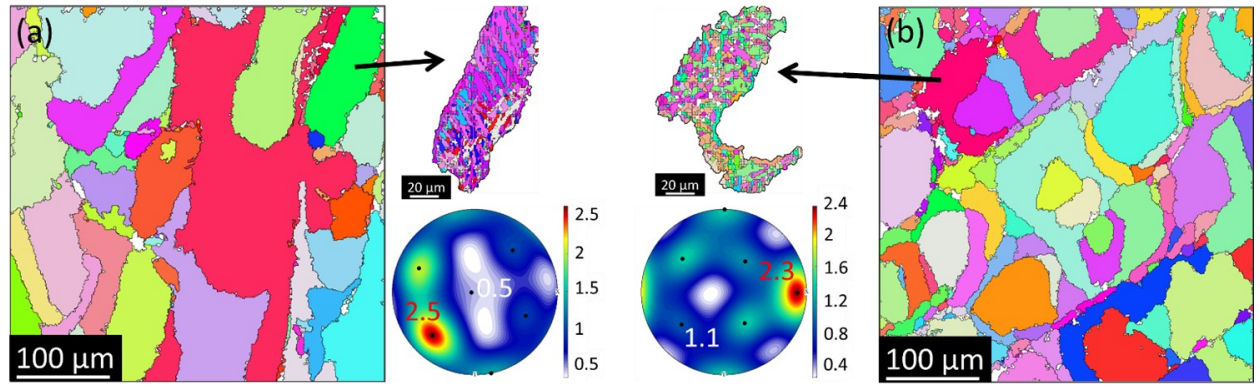


Figure 5. The reconstructed prior β orientation map of the (a) vertical and (b) horizontal cross-sections. The black arrows point to the alpha map of each selected grain after the reconstruction (of prior β), and the pole figures show the orientations of the α' laths inside the selected grains. The black dots inside the pole figures represent the six $\{110\}$ poles of the corresponding prior β grain. The strong bias towards a single pole indicates that variant selection has occurred.

The quantification of the α/α boundary variant type was performed on both cross-sections, and the results are shown in Figure 6. The type 4 α/α boundary variant constitutes the majority of the variants with a relative frequency of 35 % and 37 % in vertical and horizontal cross-sections, respectively. The type 5 α/α boundary variant was the second most frequent α/α variant with relative frequencies of 24 % and 23 % in vertical and horizontal cross-sections, respectively.

Comparing these with a relative frequency of 18.2 % for unbiased selection, it is clear that both types occur much more frequently. On the other hand, the type 2 and type 3 α/α boundary variants showed a relative frequency close to that of a randomly distributed dataset in both cross-sections.

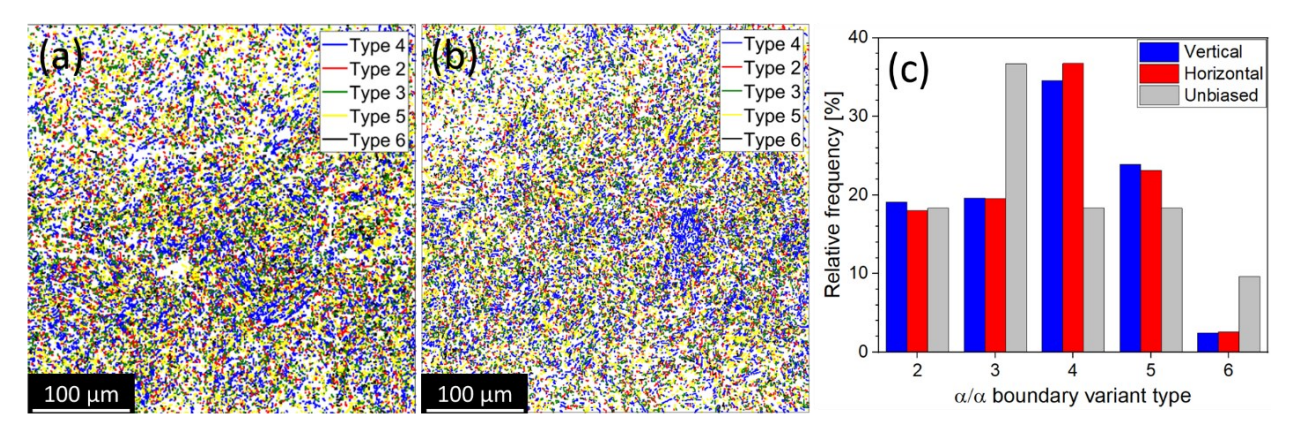


Figure 6. Distribution maps of the different α/α boundary variant types in (a) vertical and (b) horizontal cross-sections, and (c) comparison of α/α boundary variant type distribution in both cross-sections.

So far, the general variant selection phenomenon has been analyzed to show that variant selection occurs during the L-PBF process of (non-)spherical Ti-6Al-4V powder. Variant selection analysis inside the prior β grains in the vertical cross-section was performed, and the results are shown in Figure 7. The type 2 α/α boundary variant was present in both grains with its distinctive rotation of 60° about [1 1 $\overline{2}$ 0]. This type of α/α boundary variant can be identified from the pole figures based on the different (0 0 0 1) poles and a common (1 1 $\overline{2}$ 0) pole of the α' lath orientation as indicated by T2 in Figure 7a,b. The type $6\alpha/\alpha$ boundary variant was present in one of the grains and was evident from the \sim 10° rotation of the α' lath around the (0 0 0 1) axis by moving from one α' lath to the neighboring α' lath as indicated by T6 in Figure 7a,b. In addition, the type $2\alpha/\alpha$ boundary variant was present in one of the grains, which was distinguishable from the type $2\alpha/\alpha$ boundary variant based on the axis of the rotation as indicated by T3 in Figure 7a,b.

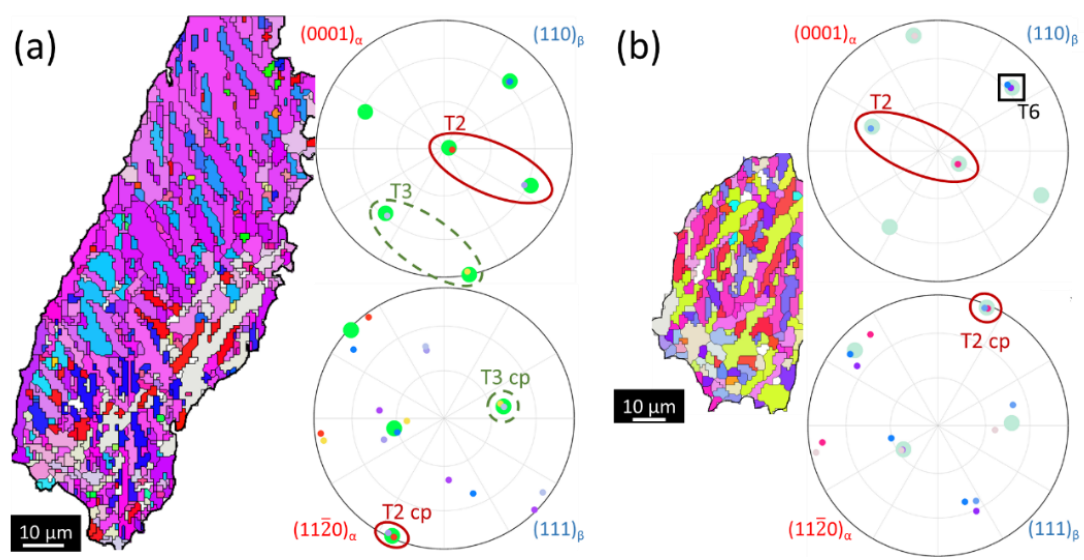


Figure 7. Detailed analysis of variant selection inside the prior β grains in the vertical cross-section showing examples of various α/α boundary types inside the grains. Larger points in all the pole figures belong to the corresponding prior β grain, and the small points are color coded with the corresponding α' lath groups in each grain. Note that the term "cp" in front of the T2 and T3 shows the common (1 1 $\bar{2}$ 0) pole.

The grain boundary precipitation of the α phase has been discussed in the α - β titanium alloys [46,47], however, α' precipitation has been assumed to be absent along prior β grain boundaries, specifically during the L-PBF process [25]. Stanford *et al.* [38] classified pairs of prior β grains into three types: (i) one common (110) pole between two adjacent β grains, (ii) close orientation between two adjacent β grains, and consequently, more than one common (110) pole, and (iii) two adjacent β grains without any special relationship. The first two types of adjacent β grains can result in variant selection during the $\beta \rightarrow \alpha$ transformation. The second type of adjacent β grain pairs and the consequent α variant selection were discussed above (Figure 8a), however, the first type of adjacent β grains and the consequent α variant selection could not be found in the current dataset (with 50 and 30 prior β grains in the horizontal and vertical cross-sections, respectively).

The detailed analysis of a grain boundary α' laths, which grew into both β grains (shown by the blue oval in Figure 8a), showed that two small α' laths with type 1 α/α boundary variant (with misorientation of $\sim 2^{\circ}$) were present on the opposite sides of the prior β grain boundary. To assess the integrity of the prior β reconstruction and validation of the grain boundary between two selected grains, the twelve variants were superimposed on the actual data. The results supported the conclusion that the drawn grain boundary had high reliability, thus, the grain boundary precipitation of the α' laths was validated once more. This finding contrasts with the findings of Simonelli *et al.* [25] who reported that regardless of the misorientation between prior β grains, no

grain boundary α' precipitation occurred during L-PBF of Ti-6Al-4V. This difference in outcome could be explained by the different powder type used in the current study. Compared to the standard powders used in L-PBF with a PSD of 15-45 µm, the "shadowing effect" [31,48] caused by non-spherical coarse powders with PSD of 50-120 μm, in which ~23 % of particles were larger than the laser spot size of 100 µm, could (slightly) alter melt pool dynamics and its stability. The instability in the keyhole, caused by laser-powder interaction and slightly lower powder packing density of non-spherical powder, could locally change the heat transfer in the interrupted melt pool. It is worth noting that the presence of β/β grain boundary α phase has been shown in L-DED processed Ti-6Al-4V parts by Carroll et al. [49]. The β/β grain boundary α phase is more prevalent in the L-DED process because of significantly lower cooling rates (i.e., 10³-10⁵ °C/s [50]) compared to the L-PBF process (i.e., $>10^9$ °C/s). The α' laths shown in Figure 8a is relatively small compared to the α lath precipitated along the β grain boundaries during the $\beta \rightarrow \alpha$ transformation. As reported in [51–53], increasing the cooling rate during $\beta \rightarrow \alpha$ transformation results in smaller α colonies and α lath width along with a higher number density of differently oriented α laths inside a single prior β grain. The L-PBF process causes melting/solidification of material once or twice in a matter of microseconds [54], causing extremely high cooling rates (i.e., > 10⁹ °C/s) inside the melt pool and during the solid-state $\beta \rightarrow \alpha$ transformation. This high cooling rate suppresses the $\beta \rightarrow \alpha$ equilibrium transformation, thus, martensitic α' laths with an average width of $\sim 1.5 \,\mu m$ grow inside the β phase with $\pm 45^{\circ}$ angle with respect to the build direction [55]. The same phenomenon was found in the horizontal cross-section between two adjacent equiaxed prior β grains, and results are shown in Figure 8b.

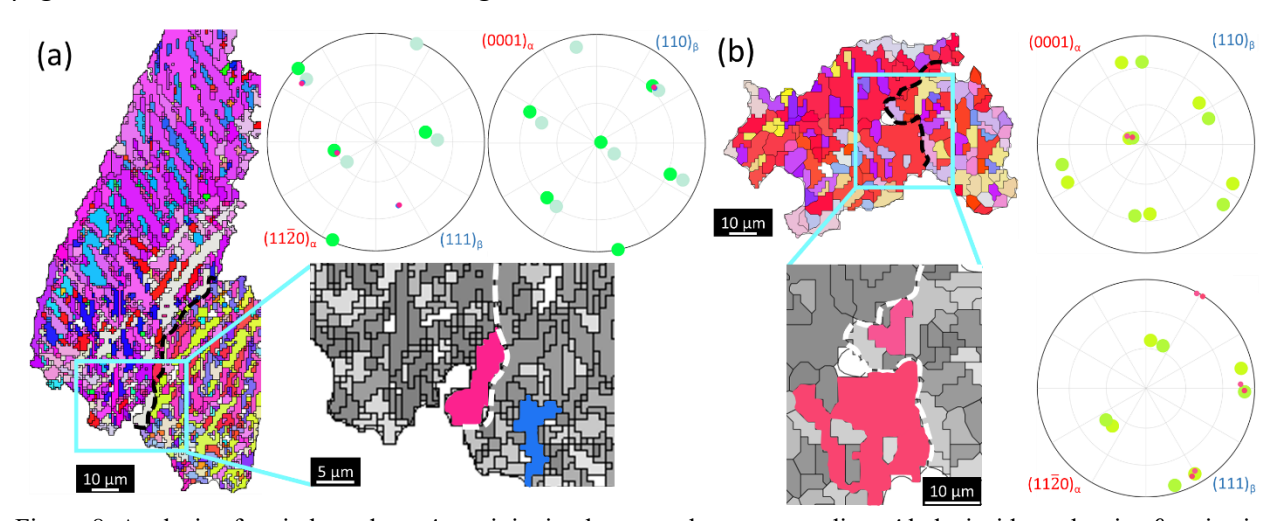


Figure 8. Analysis of grain boundary α' precipitation between the corresponding α' laths inside each prior β grains in (a) vertical and (b) horizontal cross-sections. Larger points in all the pole figures belong to the corresponding prior β

grain orientation, and the small points are color coded with the corresponding α' lath groups in each grain. The colorized α' laths in magnified images are the α' precipitation from the β/β grain boundary.

Selected grains from each cross-section were analyzed separately for the constituent α' variants based on the BOR governing the $\beta \rightarrow \alpha$ transformation, and results are shown in Figure 9. As mentioned before, if the variants were distributed randomly inside a prior β grain, the relative frequency of each variant would be 8.33 %. However, the different relative frequencies of variants suggested the presence of variant selection during L-PBF on non-spherical Ti-6Al-4V powder. Regardless of cross-section, the maximum variant relative frequency was ~16 % in all the grains. This showed that the variant selection intensity in the equiaxed or columnar grains was similar, thus, there was no orientation dependence in the L-PBF Ti-6Al-4V part. It should be noted that sample height from the base plate potentially affects the variant bias throughout the sample, hence, this will be studied in future work.

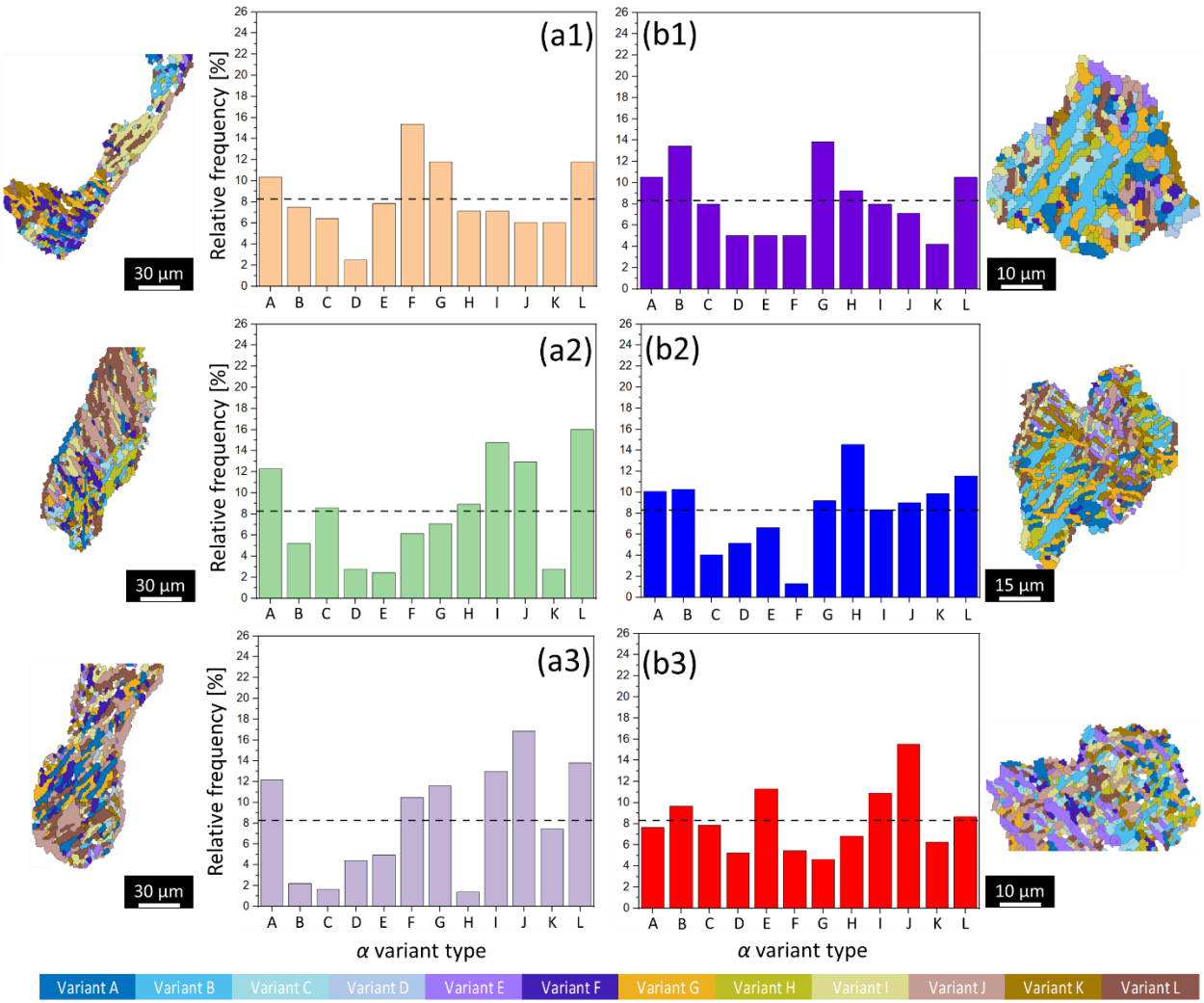


Figure 9. Relative frequency of the twelve variants in three prior beta grains from (a) vertical and (b) horizontal cross-sections. The dashlines showed the random distribution percentage of each variant (8.33 %). The α' laths in the grains were color-coded based on the colors under the figures associated with different variants.

Typically, the "shadowing effect" results in locally lower cooling rates during the L-PBF process. This effectively correlates with the size of the particle blocking the laser path. Khairallah et al. [56] showed that agglomerated small spherical powders could block the laser path and cause defects as significant as lack of fusion or end-of-track pores. To our knowledge, the hypothesis of cooling rate reduction because of the shadowing effect has not been studied quantitatively. Here, using dynamic x-ray radiography (DXR), the reduction in keyhole depth as a result of shadowing is shown, and different cooling rates are calculated using the following equation [57–59]:

$$\frac{\partial T}{\partial t} = \left[1 + \frac{\xi}{\sqrt{\xi^2 + z^2}} + \frac{2\alpha\xi}{V(\xi^2 + z^2)} \right] \left(\frac{\lambda P}{2\pi k} \frac{V^2}{2\alpha} \frac{1}{\sqrt{\xi^2 + z^2}} \right) EXP \left[-\frac{V}{2\alpha} \left(\xi + \sqrt{\xi^2 + z^2} \right) \right]$$
(Eq. 1)

where ξ is the relative distance to the center of the laser spot in the x direction defined by (x - Vt) (mm), z is the vertical distance from the center of the laser spot (mm), α is the thermal diffusivity of Ti-6Al-4V alloy (mm²/s), V is the laser scan speed (mm/s), P is the laser power (W), k is the thermal conductivity of Ti-6Al-4V alloy (W/mm·K). The keyhole depth is directly proportional to the laser power impinging on the melt pool above the threshold for keyhole formation. The keyhole depth reduction can be used to measure the effective laser power after the shadowing effect:

$$EP = P \times \frac{D}{D_{max}}$$
 (Eq. 2)

where EP is the effective laser power in W, P is the nominal laser power in W, D is the keyhole depth at the specific time in μ m, and D_{max} is the maximum keyhole depth in μ m. The constant vertical distance of 90 μ m from the top of the base plate is used in (Eq. 1) to effectively compare the effect of the shadowing phenomenon on the cooling rate in the same spot.

Figure 10 shows the DXR results in which the laser-powder interactions and dynamics of the melt pool were observed during keyhole mode laser melting of non-spherical Ti-6Al-4V powder. In each DXR frame, the cooling rate was calculated at 90 µm beneath the base plate, and the results are summarized in

Table 3. As demonstrated in Figure 10, the melt pool depth was ~149 μ m at t₀, while it decreased to ~108 μ m at t₀+12.3 ms. The keyhole depth reduction was ~ 28 % and could be related to the shadowing effect when spattered non-spherical particles block the laser path. In other words, the shadowing effect could locally lower cooling rates, thus, the β/β grain boundary α variant selection would be present. Since ~23 % of the particles have an equivalent diameter of > 100 μ m, it seems reasonable to relate the occurrence of β/β grain boundary α variant selection process to the powder morphology and resultant higher cooling rate.

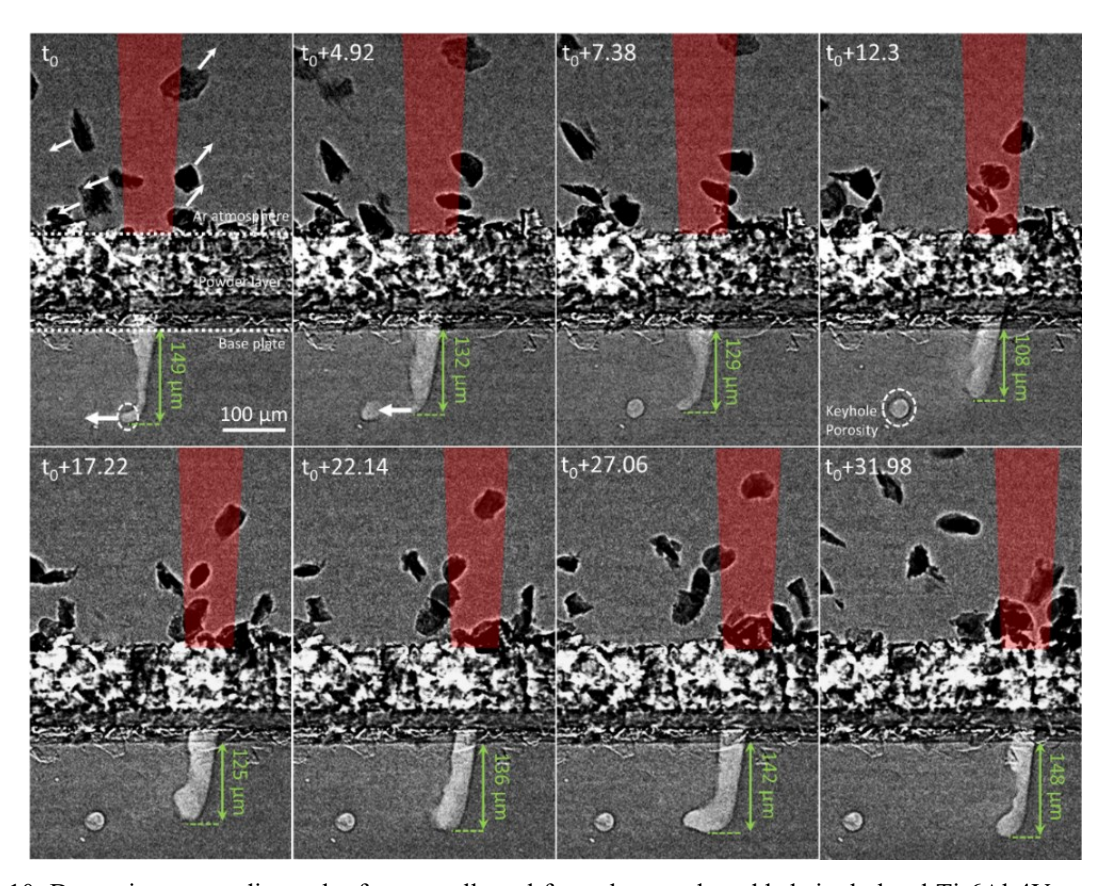


Figure 10. Dynamic x-ray radiography frames collected from the powder-added single-bead Ti-6Al-4V experiment using laser power of 350 W and a laser scan speed of 650 mm/s. Results show a keyhole pore formation, powder ejection from the powder bed as a result of laser impact, and keyhole depth reduction because of the laser shadowing phenomenon. A powder layer thickness of 200 μ m and a laser diameter of 100 μ m was used in the DXR experiments. The time unit was in ms.

Table 3. Estimated cooling rates at 90 μ m beneath the base-plate surface during the occurrence of the shadowing effect.

Time	Keyhole depth ratio $(\frac{D}{D_{max}})$	Effective laser power (<i>EP</i>)	Cooling rate
[ms]	D_{max}	[W]	[°C/s]
0	1	350	2.51×10^{5}
4.92	0.886	310	2.23×10 ⁵
7.38	0.866	303	2.18×10^{5}
12.3	0.725	253.4	1.82×10 ⁵
17.22	0.839	293.6	2.11×10 ⁵
22.14	0.913	319.5	2.29×10 ⁵
27.06	0.953	333.5	2.40×10^{5}
31.98	0.993	347.6	2.50×10^{5}

In titanium alloys, the martensitic transformation of $\beta \rightarrow \alpha'$ that occurs at a high enough cooling rate [40] is a diffusionless process with a large transformation strain that includes a large volume change. The latter means that each α' lath sets up reaction stresses against its surroundings with a consequent elastic strain energy in the material. The calculated volume changes (see

Appendix A.1, Eq. A.21) show that the principal lattice distortions are +2.2%, +10.9%, and -9.4% in the BCC parent structure aligned with $[1\bar{1}0]_{\beta}$, $[110]_{\beta}$, and $[001]_{\beta}$, respectively.

After calculating shape strains for each variant using the formulation in Appendix A.1, the results showed that the magnitude of the shape strain for all variants was the same, as expected. Each one varied, however, in the direction of the displacement (d) and the orientation of the habit plane (p), as explained in Appendix A.1 (see Eq. A.2). The shape strain of variant A (see Table 2) in the parent coordinate system for the primary basal slip system of $(1\overline{1}0)[111]$ is

```
\begin{bmatrix} 1.2068 & -0.1084 & -0.1973 \\ 0.1105 & 0.9420 & -0.1054 \\ 0.1284 & -0.0673 & 0.8774 \end{bmatrix} \text{ with the displacement direction of } d = [\overline{0.9459} \ \overline{0.5056} \ \overline{0.5876}],
```

habit plane of $p = (\overline{0.2186} \ 0.1146 \ 0.2085)$, and shape strain magnitude of 1.22.

To minimize the elastic strain energy, certain combinations of variants of α' laths can accommodate each other's strains which results in clusters of particular variants. This clustering phenomenon is called self-accommodation, which minimizes the elastic deformation at the microscopic scale and avoids shape change at the macroscopic scale [60,61]. Wang *et al.* [42] showed that two categories of cluster tend to form, each consisting of three α variants, thus, minimizing the transformation shape strain by self-accommodation. Category I comprises clusters of variants A-B-C, D-E-F, G-H-I, and J-K-L (see Table 2), and Category II comprises clusters of variants A-E-I, B-D-L, C-G-K, and F-H-J. Since the α variants in cluster Categories I and II belong to the type 2 and type 4 α/α boundary variants, respectively, the percentage of occurrence of these α/α boundary variant types can be used to determine which cluster category is dominant.

Figure 6c shows that the type 4 α/α variant was dominant, thus, cluster Category II is considered to be the dominant self-accommodation cluster. As an example of the self-accommodation phenomenon, a Category I cluster is illustrated in Figure 11a, and the corresponding α/α boundary variant type distribution inside the selected grain is displayed in Figure 11b. The dominance of the Category II cluster inside the selected grain was obvious, however, Category I clusters were present, and one of them is shown in Figure 11a. The Category I clusters were reported to be the typical category of α' laths regardless of the cooling rate during the $\beta\rightarrow\alpha$ transformation [62], however, the results from L-PBF of non-spherical Ti-6Al-4V powder suggested that the Category II clusters dominated in this case. This observation was related to the cooling rate during L-PBF in agreement with Ref. [24,63]. Generally, high cooling rate

results in large residual stress because the equilibrium $\beta \rightarrow \alpha$ transformation is suppressed and is replaced by the diffusionless $\beta \rightarrow \alpha'$ transformation. This residual stress favors the nucleation of certain variants over others, thus, exaggerating variant selection [64]. As reported by Zhang et al. [65], any applied shear stress or internal residual stress affects the variant selection process. Also, Shi et al. [66] used phase-field simulation and showed that applying shear stress along a specific direction biased the $\beta \rightarrow \alpha$ transformation and increased variant selection. Herein, under high cooling rate conditions in L-PBF processed non-spherical Ti-6Al-4V powder, Category II clusters dominated. To quantify the amount of shape strain minimization, the corresponding shape strains for each variant were multiplied together and resulted in the shape strain of **F0.908** -0.407for Categories I and II, and 0.145 L0.395 0.185

respectively. The calculations showed a significant reduction of shape strain by the occurrence of Category II clusters compared to Category I. Note that the Category I clusters even increased the shear and dilatation components of the shape strain, leading to a lower frequency of Category I clusters.

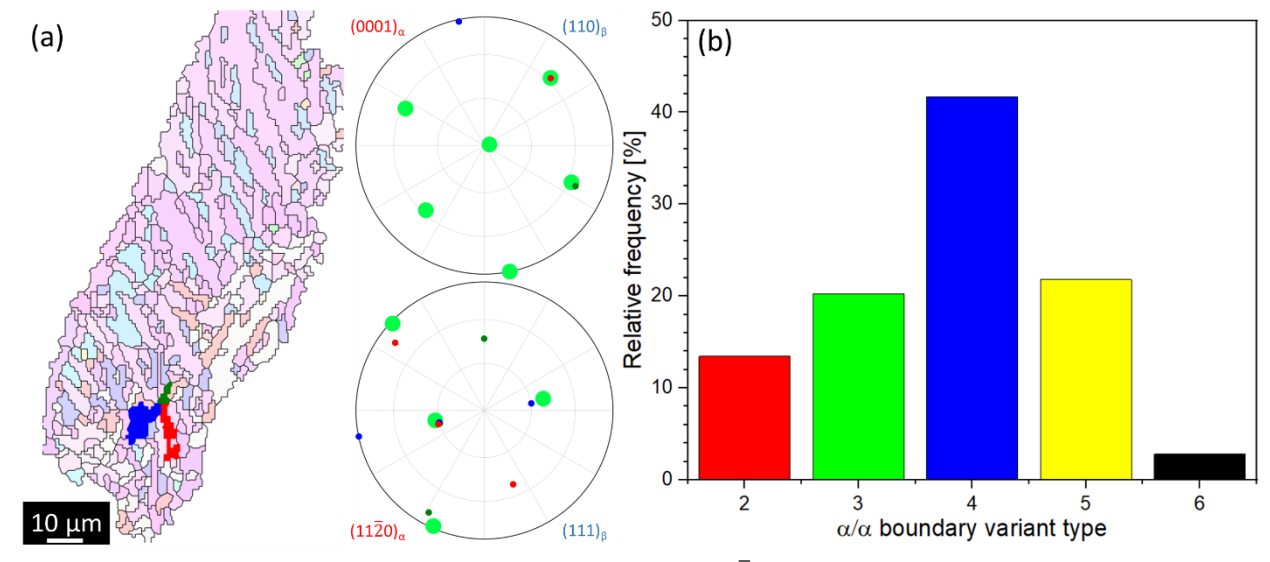


Figure 11. (a) A cluster of three α' lath variants sharing a $[11\bar{2}0]$ pole, characteristics of a Category I self-accommodation, and (b) the corresponding distribution of α/α boundary variant inside the prior β grain shown in (a). Larger points in all the pole figures belong to the corresponding prior β grain orientation, and the small points are color coded with the corresponding α' lath groups in each grain.

Now that the general occurrence and the presence of each type of variant selection inside the L-PBF processed non-spherical Ti-6Al-4V powder has been discussed, we assess the degree of variant selection (DVS) inside each cross-section using the following equation [67]:

$$DVS = \sum_{i}^{6} |P_{theoretical} - P_{experimental}|$$
 (Eq. 3)

Here $P_{theoretical}$ is the relative frequency of each α/α boundary variant type in the condition of random distribution, $P_{experimental}$ is the experimentally measured relative frequency of each α/α boundary variant type, and i is the variant type counter which can take integer values from one to six. If no variant selection is present, DVS is zero, and if just one variant is present inside the prior β grain, DVS is 1.833. The calculated DVS was found to be 0.57 and 0.54 for horizontal and vertical cross-sections, respectively. The small difference suggests that the variant selection phenomenon is independent of orientation inside the prior β grain. Any difference between the horizontal and vertical cross-sections would be merely statistical.

The present work included the effect of non-spherical powder with PSD of 50-120 µm compared to the spherical powder with PSD of 15-45 µm on the texture evolution of the L-PBF processed Ti-6Al-4V. The general idea was that high cooling rates in L-PBF suppress some specific variant selection processes. However, here it was shown that the locally lower cooling rates during L-PBF of particles larger than laser beam diameter could slightly change the variant selection mechanism. The following points require further study:

- Effect of the L-PBF processing parameters such as laser power, scan speed, hatch spacing, and scanning strategy on the variant selection.
- Role of build height, pre-heat temperature, and *in-situ* heat treatment due to consecutive thermal cycles on the variant selection.

4. Conclusion

This study focused on manufacturing of Ti-6Al-4V parts through L-PBF processing of non-spherical powder and the occurrence of the alpha on prior beta grain boundaries. The potential effect of powder characteristics on β/β grain boundary α' phase was studied which was previously assumed to be absent in the L-PBF processed Ti-6Al-4V parts because of the high cooling rates. The following conclusions were drawn:

• The presence of β/β grain boundary α' phase was demonstrated using EBSD. This contrast with other literature was justified using synchrotron X-ray high-speed imaging and keyhole instability analysis. Locally lower cooling rates were detected under special circumstances

- of keyhole depth reduction due to the "shadowing effect," which increased the chance of initial grain boundary α' nucleation.
- The prevalent mechanism of variant selection was self-accommodation and the most abundant α/α grain boundary variant was type 4 (63.26° // [10 5 5 3]) with a frequency of ~36% which was in agreement with the frequencies (35-40%) reported in the literature for the Ti-6Al-4V alloy fabricated using process with extremely high cooling rates (e.g., L-PBF).
- The phenomenological theory of martensite transformation was used to calculate (i) the shape strain needed for the β→α' transformation and (ii) the amount of shape strain minimization caused by self-accommodation clustering. The results showed the dominance of Category II clusters associated with the type 4 α/α grain boundary variant.

The influence of processing parameters and build height on the evolution of microstructure and variant selection phenomenon in the L-PBF processed non-spherical Ti-6Al-4V powder requires further assessment.

Acknowledgments

AM acknowledges startup funding from the Mechanical, Materials, and Aerospace Engineering Department at the Illinois Institute of Technology in Chicago, Illinois. Also, this work is supported in part by the Pennsylvania Infrastructure Technology Alliance, a partnership of Carnegie Mellon, Lehigh University, and the Commonwealth of Pennsylvania's Department of Community and Economic Development (DCED). The authors recognize Reading Alloys (formerly affiliated with AMETEK Inc., now a part of Kymera International), especially Muktesh Paliwal and Mike Marucci, for providing the Ti-6Al-4V powder used in this work and assistance with the study. This work was performed under the auspices of the U.S. Department of Energy by Lawrence Livermore National Laboratory under contract DE-AC52-07NA27344 and IM release number # LLNL-JRNL-834760. The authors acknowledge partial support from the National Science Foundation under grant number DMR-2050916. IG appreciates the financial support from the Gallogly College of Engineering at the University of Oklahoma.

Appendix A.1: Martensitic transformation and shape strain calculations

In theory, the martensitic transformation of BCC to HCP is based on the fact that the interface between them should be macroscopically invariant (i.e., invariant plane strain (IPS))

because this transformation is diffusionless and the interface between parent and product phases should be highly coherent [68]. This transformation consists of three components; (i) the Bain transformation B to convert the parent lattice (BCC) to the product lattice (HCP), (ii) an inhomogeneous shear P', aka complementary shear, in the converted lattice to provide an undistorted plane, and (iii) a rigid body rotation R to keep bringing back the interface line to the invariant condition. There have been different approaches to formulating the martensitic transformation by Bowles et al. [69] and Wechsler [70]. Here, the calculations from [69] are used because of the conciseness of their formulation. The total shape deformation can then be expressed as:

$$P = RBP' (Eq. A.1)$$

where P is an invariant plane strain in the habit plane, which is the interface between the parent and product phases, R is the rigid body rotation, B is the Bain transformation, and P' is the complementary shear. Using this equation, the total deformation during the martensitic deformation can be calculated. Bain transformation is known based on the lattice correspondence, and rigid body rotation is known based on the relationship between the two different coordinate frames. Thus, by having the complementary shear, the total deformation can be calculated. This complementary shear is a slip or twinning system in the HCP phase expressed in the parent phase coordinate system and selected based on the most common slip systems for the crystal structure. Because both P and P' are in the form of IPS, they can be expressed using the following equations:

$$P = I + d \cdot p \tag{Eq. A.2}$$

$$P' = I + d' \cdot p' \tag{Eq. A.3}$$

where I is a unit matrix, p is the unit vector normal to the habit plane, d is the vector showing the direction of displacement, which includes the magnitude of strain as well, p' is the unit vector normal to the complementary shear plane, d' is the vector perpendicular to the complementary shear which includes the magnitude of shear as well. The nearly parallel slip systems in the BCC-Ti and HCP-Ti can produce a complementary shear. There are four crystallographically different slip systems in the HCP-Ti that are nearly parallel to the slip systems in the BCC-Ti:

$$1: (\overline{1}101)[\overline{1}2\overline{1}\overline{3}]_{\alpha} \parallel (0\overline{1}1)[\overline{1}11]_{\beta}$$

$$2{:}\; (0001)[11\overline{2}0]_\alpha \, \| \, (1\overline{1}0)[111]_\beta$$

3:
$$(\overline{1}101)[11\overline{2}0]_{\alpha} \parallel (0\overline{1}1)[111]_{\beta}$$

4:
$$(\overline{1}100)[11\overline{2}0]_{\alpha} \parallel (\overline{1}\overline{1}2)[111]_{\beta}$$

If we take, for example, slip system 1 to be the acting slip system, p' will be $(0\overline{1}1)$. To calculate the invariant line of the interface of the parent and product phases, a unit vector parallel to the invariant line is assumed. This unit vector is expressed as $X = [X_1 \ X_2 \ X_3]$ in the parent phase coordinate system and as $x = [x_1 \ x_2 \ x_3]$ in the product phase coordinate system. Similarly, the invariant plane containing the displacement vectors of P and P' is assumed and expressed by $N = (N_1 \ N_2 \ N_3)$ and $n = (n_1 \ n_2 \ n_3)$ in the parent and product phases coordinate systems, respectively. X and X are related by the Bain transformation:

$$x = B \cdot X$$
 (Eq. A.4)

There are certain conditions that help to solve and find the unit vector X. Firstly, the length of X and x are unchanged, thus:

$$X_1^2 + X_2^2 + X_3^2 = 1$$
 (Eq. A.5)

$$x_1^2 + x_2^2 + x_3^2 = 1$$
 (Eq. A.6)

And by substituting Eq. A.4 in Eq. A.6:

$$\eta_1^2 \cdot x_1^2 + \eta_2^2 \cdot x_2^2 + \eta_3^2 \cdot x_3^2 = 1$$
 (Eq. A.7)

Secondly, the complementary shear plane $p' = (p'_1 p'_2 p'_3)$ contains the invariant line, thus:

$$p'.X = p'_1 \cdot X_1 + p'_2 \cdot X_2 + p'_3 \cdot X_3 = 0$$
 (Eq. A.8)

Similarly, *N* and *n* are related by the Bain transformation:

$$N = B \cdot n \tag{Eq. A.9}$$

Again, because the length of the plane normal is unchanged:

$$N_1^2 + N_2^2 + N_3^2 = 1$$
 (Eq. A.10)

$$n_1^2 + n_2^2 + n_3^2 = 1$$
 (Eq. A.11)

And by substituting Eq. A.9 in Eq. A.11:

$$\frac{x_1^2}{\eta_1^2} + \frac{x_2^2}{\eta_2^2} + \frac{x_3^2}{\eta_2^2} = 1$$
 (Eq. A.12)

Plane N contains the complementary shear direction d', thus:

$$d' \cdot N = d'_1 \cdot N_1 + d'_2 \cdot N_2 + d'_3 \cdot N_3 = 0$$
 (Eq. A.13)

By using Eq. A.5, Eq. A.7, and Eq. A.8, the invariant line X can be calculated and by using Eq. A.10, Eq. A.12, and Eq. A.13, the invariant plane N can be calculated. There are two possible solutions for X, and two possible solutions for N, resulting in four combinations of possible invariant lines and planes. The combination with the smallest shape strain and simple shear values was suggested to be appropriate [71].

Both *n* and *x* need to be brought back to their initial position to have an invariant line interface. A rigid body rotation can be applied to achieve this:

$$X = x \cdot R \tag{Eq. A.14}$$

$$N = n \cdot R \tag{Eq. A.15}$$

Also, the outer product of the invariant plane normal and invariant line should be brought back by *R*:

$$(N \times X) = (n \times x) \cdot R \tag{Eq. A.16}$$

It is of great importance to note that all the parameters (B, R, X, and N) are defined in the orthorhombic coordinate system, O, and they need to be expressed in the BCC coordinate system. The transformation matrix T can be used to do this, which is expressed as follows if the $(100)[011]_O \parallel (1\overline{1}0)[111]_\beta$ is selected:

$$T = \begin{bmatrix} 1/\sqrt{2} & 1/\sqrt{2} & 0 \\ -1/\sqrt{2} & 1/\sqrt{2} & 0 \\ 0 & 0 & 1 \end{bmatrix}$$
 (Eq. A.17)

By using transformation matrix T, the parameters can be expressed in the BCC coordinate system instead of an orthorhombic coordinate system using the following series of equations:

$$u = T \cdot X, h = N \cdot T^{-1}, R_b = T^{-1} \cdot R \cdot T, B_b = T^{-1} \cdot B \cdot T$$
 (Eq. A.18)

where u, h, R_b , and B_b are the parameters in the BCC coordinate system corresponding to the X, N, R, and B in the HCP coordinate system, respectively. After finding the u, h, R_b , and B_b , the following equations can be used to calculate the elements of shape strain P [71]:

$$p = p' \cdot (R_b B_b)^{-1} - p'$$
 (Eq. A.19)

$$d = ((R_b B_b) \cdot d' - d')/(p \cdot d')$$
 (Eq. A.20)

Finally, the total shape deformation *P* can be calculated using Eq. A.2.

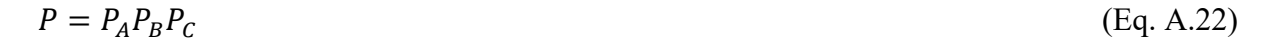
The choice of lattice correspondence to convert the BCC to HCP is based on the minimization of distortion and rotation of the lattice vectors. One of the orientation relationships other than the aforementioned BOR is the Pitsch-Schrader orientation relationship which is defined as $[1\bar{1}0]_{\beta}||[0001]_{\alpha}$, $[110]_{\beta}||[10\bar{1}0]_{\alpha}$, and $[001]_{\beta}||[\bar{1}2\bar{1}0]_{\alpha}$. In order to simplify the calculations, the Pitsch-Schrader orientation relationship can be expressed in the orthohexagonal system, which shows the relationship between the BCC and orthorhombic lattices as $[1\bar{1}0]_{\beta}||[100]_{0}$, $[110]_{\beta}||[010]_{0}$, and $[001]_{\beta}||[001]_{0}$ [72]. The most basic Bain transformation was originally developed for the FCC to BCC transformation. Here, by using the Pitsch-Schrader orientation relationship, the Bain transformation B for the case of BCC to HCP in the orthohexagonal system can be expressed as follows:

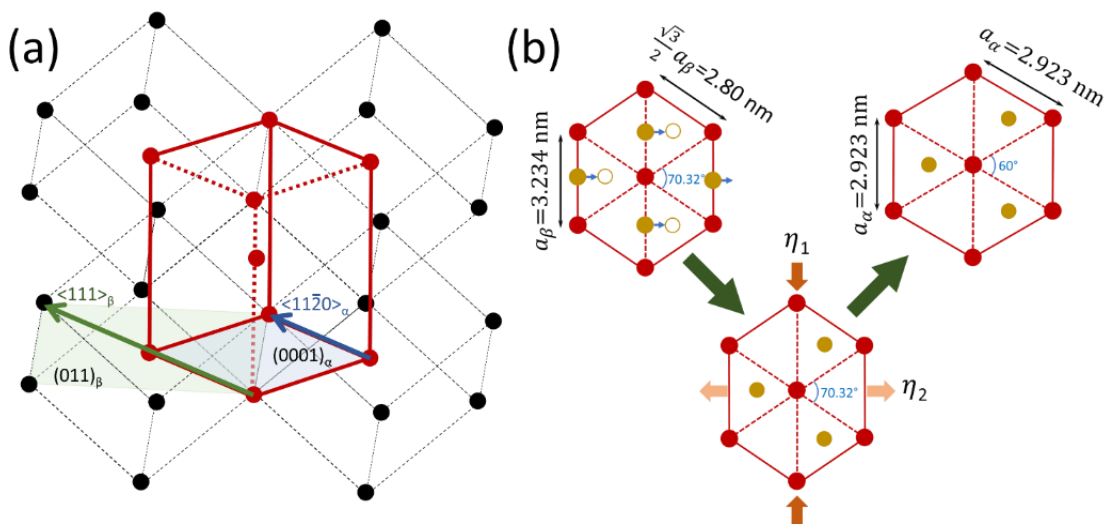
$$B = \begin{bmatrix} \eta_1 & 0 & 0 \\ 0 & \eta_2 & 0 \\ 0 & 0 & \eta_3 \end{bmatrix} = \begin{bmatrix} \frac{c_\alpha}{\sqrt{2}a_\beta} & 0 & 0 \\ 0 & \frac{\sqrt{3}a_\alpha}{\sqrt{2}a_\beta} & 0 \\ 0 & 0 & \frac{a_\alpha}{a_\beta} \end{bmatrix} = \begin{bmatrix} 1.022 & 0 & 0 \\ 0 & 1.109 & 0 \\ 0 & 0 & 0.9055 \end{bmatrix}$$
(Eq. A.21)

where a_{β} is the lattice parameter of β phase (3.23 Å), a_{α} and c_{α} are the lattice parameters of α phase (2.925 Å and 4.668 Å, respectively, see supplementary Fig. 1), and η_1 , η_2 , and η_3 are the principal lattice distortion in the orthohexagonal system.

Up until this point of calculations, the type of α variant produced from the β phase did not have any effect because the nature of transformation for every variant is basically a BCC to HCP transformation, thus, the Bain transformation matrix B would be the same and only dependent on the lattice parameters. It should be noted that the direction of each principal lattice distortion would change based on the variant type, but still, the magnitude of distortion would be constant.

By multiplication of corresponding shape strain of each variant in each self-accommodation cluster, the amount of shape strain after the self-accommodation process can be calculated. For example, for the cluster of A, B, and C variants, the shape strain can be calculated using the following equation:





Supplementary Fig. 1. (a) Schematic of the Burgers orientation relationship (BOR) between the BCC and HCP showing the corresponding planes and directions, and (b) schematic of the necessary dilation and compression to convert the BCC to HCP. The lattice parameters were measured using X-ray diffraction pattern on the L-PBF processed non-spherical Ti-6Al-4V powder [31] and Rietveld refinement method.

References

- [1] W.G. Burgers, On the process of transition of the cubic-body-centered modification into the hexagonal-close-packed modification of zirconium, Physica. 1 (1934) 561–586.
- [2] B.J. Hayes, B.W. Martin, B. Welk, S.J. Kuhr, T.K. Ales, D.A. Brice, I. Ghamarian, A.H. Baker, C. V Haden, D.G. Harlow, H.L. Fraser, P.C. Collins, Predicting tensile properties of Ti-6Al-4V produced via directed energy deposition, Acta Mater. 133 (2017) 120–133.
- [3] S.S. Al-Bermani, M.L. Blackmore, W. Zhang, I. Todd, The Origin of Microstructural Diversity, Texture, and Mechanical Properties in Electron Beam Melted Ti-6Al-4V, Metall. Mater. Trans. A. 41 (2010) 3422–3434.
- [4] X. Jiang, B.P. Wynne, J. Martin, Variant selection in stationary shoulder friction stir welded Ti-6Al-4V alloy, J. Mater. Sci. Technol. 34 (2018) 198–208.
- [5] J. Romero, M. Preuss, J. Quinta da Fonseca, Texture memory and variant selection during phase transformation of a zirconium alloy, Acta Mater. 57 (2009) 5501–5511.
- [6] L. Lei, Q. Zhao, C. Wu, Y. Zhao, S. Huang, W. Jia, W. Zeng, Variant selection, coarsening behavior of α phase and associated tensile properties in an α+β titanium alloy, J. Mater. Sci. Technol. 99 (2022) 101–113.
- [7] S.L. Lu, H.P. Tang, S.M.L. Nai, Y.Y. Sun, P. Wang, J. Wei, M. Qian, Intensified texture in selective electron beam melted Ti-6Al-4V thin plates by hot isostatic pressing and its fundamental influence on tensile fracture and properties, Mater. Charact. 152 (2019) 162–168.
- [8] Q. Luo, Y. Guo, B. Liu, Y. Feng, J. Zhang, Q. Li, K. Chou, Thermodynamics and kinetics of phase transformation in rare earth–magnesium alloys: A critical review, J. Mater. Sci. Technol. 44 (2020) 171–190.
- [9] Y. Pang, D. Sun, Q. Gu, K.-C. Chou, X. Wang, Q. Li, Comprehensive Determination of

- Kinetic Parameters in Solid-State Phase Transitions: An Extended Jonhson–Mehl–Avrami–Kolomogorov Model with Analytical Solutions, Cryst. Growth Des. 16 (2016) 2404–2415.
- [10] D. Bhattacharyya, G.B. Viswanathan, R. Denkenberger, D. Furrer, H.L. Fraser, The role of crystallographic and geometrical relationships between α and β phases in an α/β titanium alloy, Acta Mater. 51 (2003) 4679–4691.
- [11] G.C. Obasi, S. Birosca, J. Quinta da Fonseca, M. Preuss, Effect of β grain growth on variant selection and texture memory effect during $\alpha \rightarrow \beta \rightarrow \alpha$ phase transformation in Ti–6 Al–4 V, Acta Mater. 60 (2012) 1048–1058.
- [12] C. Cayron, Importance of the $\alpha \rightarrow \beta$ transformation in the variant selection mechanisms of thermomechanically processed titanium alloys, Scr. Mater. 59 (2008) 570–573.
- [13] E. Farabi, P.D. Hodgson, G.S. Rohrer, H. Beladi, Five-parameter intervariant boundary characterization of martensite in commercially pure titanium, Acta Mater. 154 (2018) 147–160.
- [14] S.M.C. van Bohemen, A. Kamp, R.H. Petrov, L.A.I. Kestens, J. Sietsma, Nucleation and variant selection of secondary α plates in a β Ti alloy, Acta Mater. 56 (2008) 5907–5914.
- [15] N. Miyano, T. Norimura, T. Inaba, K. Ameyama, Reasons for Formation of Triangular α Precipitates in Ti-15V-3Cr-3Sn-3Al & β Titanium Alloy, Mater. Trans. 47 (2006) 341–347.
- [16] S. Balachandran, A. Kashiwar, A. Choudhury, D. Banerjee, R. Shi, Y. Wang, On variant distribution and coarsening behavior of the α phase in a metastable β titanium alloy, Acta Mater. 106 (2016) 374–387.
- [17] Y. Dong, X. Liu, J. Zou, Y. Ke, P. Liu, L. Ma, H. Luo, Effect of cooling rate following β forging on texture evolution and variant selection during β → α transformation in Ti-55511 alloy, J. Mater. Sci. Technol. 113 (2022) 1–13.
- [18] S.C. Vogel, D. Bhattacharyya, G.B. Viswanathan, D.J. Williams, H.L. Fraser, Phase Transformation Textures in Ti-6Al-4V Alloy, Mater. Sci. Forum. 495–497 (2005) 681–686.
- [19] S. Hémery, A. Naït-Ali, M. Guéguen, J. Wendorf, A.T. Polonsky, M.P. Echlin, J.C. Stinville, T.M. Pollock, P. Villechaise, A 3D analysis of the onset of slip activity in relation to the degree of micro-texture in Ti–6Al–4V, Acta Mater. 181 (2019) 36–48.
- [20] S.L. Semiatin, K.T. Kinsel, A.L. Pilchak, G.A. Sargent, Effect of Process Variables on Transformation-Texture Development in Ti-6Al-4V Sheet Following Beta Heat Treatment, Metall. Mater. Trans. A. 44 (2013) 3852–3865.
- [21] T. Furuhara, T. Maki, Variant selection in heterogeneous nucleation on defects in diffusional phase transformation and precipitation, Mater. Sci. Eng. A. 312 (2001) 145–154.
- [22] Z.B. Zhao, Q.J. Wang, Q.M. Hu, J.R. Liu, B.B. Yu, R. Yang, Effect of β (110) texture intensity on α -variant selection and microstructure morphology during $\beta \rightarrow \alpha$ phase transformation in near α titanium alloy, Acta Mater. 126 (2017) 372–382.
- [23] R. DeMott, P. Collins, C. Kong, X. Liao, S. Ringer, S. Primig, 3D electron backscatter diffraction study of α lath morphology in additively manufactured Ti-6Al-4V, Ultramicroscopy. 218 (2020) 113073.
- [24] P.L. Stephenson, N. Haghdadi, R. DeMott, X.Z. Liao, S.P. Ringer, S. Primig, Effect of scanning strategy on variant selection in additively manufactured Ti-6Al-4V, Addit. Manuf. 36 (2020) 101581.

- [25] M. Simonelli, Y.Y. Tse, C. Tuck, On the Texture Formation of Selective Laser Melted Ti-6Al-4V, Metall. Mater. Trans. A. 45 (2014) 2863–2872.
- [26] R.R. Kamath, P. Nandwana, Y. Ren, H. Choo, Solidification texture, variant selection, and phase fraction in a spot-melt electron-beam powder bed fusion processed Ti-6Al-4V, Addit. Manuf. 46 (2021) 102136.
- [27] Y.P. Dong, Y.L. Li, S.Y. Zhou, Y.H. Zhou, M.S. Dargusch, H.X. Peng, M. Yan, Costaffordable Ti-6Al-4V for additive manufacturing: Powder modification, compositional modulation and laser in-situ alloying, Addit. Manuf. 37 (2020) 101699.
- [28] W. Ding, G. Chen, M. Qin, Y. He, X. Qu, Low-cost Ti powders for additive manufacturing treated by fluidized bed, Powder Technol. 350 (2019) 117–122.
- [29] Q. Tao, Z. Wang, G. Chen, W. Cai, P. Cao, C. Zhang, W. Ding, X. Lu, T. Luo, X. Qu, M. Qin, Selective laser melting of CP-Ti to overcome the low cost and high performance trade-off, Addit. Manuf. 34 (2020) 101198.
- [30] Z. Wu, M. Asherloo, R. Jiang, M.H. Delpazir, N. Sivakumar, M. Paliwal, J. Capone, B. Gould, A. Rollett, A. Mostafaei, Study of printability and porosity formation in laser powder bed fusion built hydride-dehydride (HDH) Ti-6Al-4V, Addit. Manuf. 47 (2021) 102323.
- [31] M. Asherloo, Z. Wu, M.H. Delpazir, E. Ghebreiesus, S. Fryzlewicz, R. Jiang, B. Gould, M. Heim, D. Nelson, M. Marucci, M. Paliwal, A.D. Rollett, A. Mostafaei, Laser-beam powder bed fusion of cost-effective non-spherical hydride-dehydride Ti-6Al-4V alloy, Addit. Manuf. 56 (2022) 102875.
- [32] A. Mostafaei, C. Zhao, Y. He, S. Reza Ghiaasiaan, B. Shi, S. Shao, N. Shamsaei, Z. Wu, N. Kouraytem, T. Sun, J. Pauza, J. V Gordon, B. Webler, N.D. Parab, M. Asherloo, Q. Guo, L. Chen, A.D. Rollett, Defects and anomalies in powder bed fusion metal additive manufacturing, Curr. Opin. Solid State Mater. Sci. 26 (2022) 100974.
- [33] M. Asherloo, Z. Wu, M. Heim, D. Nelson, M. Paliwal, A.D. Rollett, A. Mostafaei, Fatigue performance of laser powder bed fusion hydride-dehydride Ti-6Al-4V powder, Addit. Manuf. 59 (2022) 103117.
- [34] J. Varela, E. Arrieta, M. Paliwal, M. Marucci, J.H. Sandoval, J.A. Gonzalez, B. McWilliams, L.E. Murr, R.B. Wicker, F. Medina, Investigation of Microstructure and Mechanical Properties for Ti-6Al-4V Alloy Parts Produced Using Non-Spherical Precursor Powder by Laser Powder Bed Fusion, Mater. . 14 (2021).
- [35] J.J. Lewandowski, M. Seifi, Metal Additive Manufacturing: A Review of Mechanical Properties, Annu. Rev. Mater. Res. 46 (2016) 151–186.
- [36] N. Sanaei, A. Fatemi, Defects in additive manufactured metals and their effect on fatigue performance: A state-of-the-art review, Prog. Mater. Sci. 117 (2021) 100724.
- [37] F. Bachmann, R. Hielscher, H. Schaeben, Texture Analysis with MTEX Free and Open Source Software Toolbox, Solid State Phenom. 160 (2010) 63–68.
- [38] N. Stanford, P.S. Bate, Crystallographic variant selection in Ti–6Al–4V, Acta Mater. 52 (2004) 5215–5224.
- [39] J. Yang, H. Yu, J. Yin, M. Gao, Z. Wang, X. Zeng, Formation and control of martensite in Ti-6Al-4V alloy produced by selective laser melting, Mater. Des. 108 (2016) 308–318.
- [40] S.A. Oh, R.E. Lim, J.W. Aroh, A.C. Chuang, B.J. Gould, B. Amin-Ahmadi, J. V. Bernier, T. Sun, P.C. Pistorius, R.M. Suter, A. D.Rollett, High speed synchrotron X-ray diffraction experiments resolve microstructure and phase transformation in laser processed Ti-6Al-4V, Mater. Res. Lett. 9 (2021) 429–436.

- [41] Y. Xu, Corrosion Behavior of Direct Metal Laser Sintered Ti-6Al-4V for Orthopedic Applications, 2021.
- [42] S.C. Wang, M. Aindow, M.J. Starink, Effect of self-accommodation on α/α boundary populations in pure titanium, Acta Mater. 51 (2003) 2485–2503.
- [43] G. Zhang, N. Li, J. Gao, H. Xiong, H. Yu, H. Yuan, Wire-fed electron beam directed energy deposition of Ti–6Al–2Zr–1Mo–1V alloy and the effect of annealing on the microstructure, texture, and anisotropy of tensile properties, Addit. Manuf. 49 (2022) 102511.
- [44] S.L. Lu, C.J. Todaro, Y.Y. Sun, T. Song, M. Brandt, M. Qian, Variant selection in additively manufactured alpha-beta titanium alloys, J. Mater. Sci. Technol. 113 (2022) 14–21.
- [45] A.A. Antonysamy, J. Meyer, P.B. Prangnell, Effect of build geometry on the β-grain structure and texture in additive manufacture of Ti6Al4V by selective electron beam melting, Mater. Charact. 84 (2013) 153–168.
- [46] R. Shi, V. Dixit, G.B. Viswanathan, H.L. Fraser, Y. Wang, Experimental assessment of variant selection rules for grain boundary α in titanium alloys, Acta Mater. 102 (2016) 197–211.
- [47] R. Shi, V. Dixit, H.L. Fraser, Y. Wang, Variant selection of grain boundary α by special prior β grain boundaries in titanium alloys, Acta Mater. 75 (2014) 156–166.
- [48] S.A. Khairallah, A.A. Martin, J.R.I. Lee, G. Guss, N.P. Calta, J.A. Hammons, M.H. Nielsen, K. Chaput, E. Schwalbach, M.N. Shah, M.G. Chapman, T.M. Willey, A.M. Rubenchik, A.T. Anderson, Y.M. Wang, M.J. Matthews, W.E. King, Controlling interdependent meso-nanosecond dynamics and defect generation in metal 3D printing, Science (80-.). 368 (2020) 660–665.
- [49] B.E. Carroll, T.A. Palmer, A.M. Beese, Anisotropic tensile behavior of Ti–6Al–4V components fabricated with directed energy deposition additive manufacturing, Acta Mater. 87 (2015) 309–320.
- [50] D.-G. Ahn, Directed Energy Deposition (DED) Process: State of the Art, Int. J. Precis. Eng. Manuf. Technol. 8 (2021) 703–742.
- [51] T. Karthikeyan, A. Dasgupta, R. Khatirkar, S. Saroja, I. Samajdar, M. Vijayalakshmi, Effect of cooling rate on transformation texture and variant selection during $\beta \rightarrow \alpha$ transformation in Ti–5Ta–1.8Nb alloy, Mater. Sci. Eng. A. 528 (2010) 549–558.
- [52] X.J. Tian, S.Q. Zhang, H.M. Wang, The influences of anneal temperature and cooling rate on microstructure and tensile properties of laser deposited Ti–4Al–1.5Mn titanium alloy, J. Alloys Compd. 608 (2014) 95–101.
- [53] D. He, J.C. Zhu, S. Zaefferer, D. Raabe, Y. Liu, Z.L. Lai, X.W. Yang, Influences of deformation strain, strain rate and cooling rate on the Burgers orientation relationship and variants morphology during β→α phase transformation in a near α titanium alloy, Mater. Sci. Eng. A. 549 (2012) 20–29.
- [54] C. Zhao, K. Fezzaa, R.W. Cunningham, H. Wen, F. De Carlo, L. Chen, A.D. Rollett, T. Sun, Real-time monitoring of laser powder bed fusion process using high-speed X-ray imaging and diffraction, Sci. Rep. 7 (2017) 1–11.
- [55] B. Vrancken, L. Thijs, J.P. Kruth, J. Van Humbeeck, Heat treatment of Ti6Al4V produced by Selective Laser Melting: Microstructure and mechanical properties, J. Alloys Compd. 541 (2012) 177–185.
- [56] K.S. A., M.A. A., L.J.R. I., G. Gabe, C.N. P., H.J. A., N.M. H., C. Kevin, S. Edwin, S.M.

- N., C.M. G., W.T. M., R.A. M., A.A. T., W.Y. Morris, M.M. J., K.W. E., Controlling interdependent meso-nanosecond dynamics and defect generation in metal 3D printing, Science (80-.). 368 (2020) 660–665.
- [57] P. Promoppatum, S.-C. Yao, P.C. Pistorius, A.D. Rollett, A Comprehensive Comparison of the Analytical and Numerical Prediction of the Thermal History and Solidification Microstructure of Inconel 718 Products Made by Laser Powder-Bed Fusion, Engineering. 3 (2017) 685–694.
- [58] D. Rosenthal, Mathematical theory of heat distribution during welding and cutting, Weld. J. 20 (1941) 220–234.
- [59] R. Fabbro, Melt pool and keyhole behaviour analysis for deep penetration laser welding, J. Phys. D. Appl. Phys. 43 (2010) 445501.
- [60] K. Bhattacharya, Self-accommodation in martensite, Arch. Ration. Mech. Anal. 120 (1992) 201–244.
- [61] J. Ma, Y. Zhang, J. Li, Z. Wang, J. Wang, Variant selection within one β grain in laser solid formed Ti-6Al-4V alloys, Mater. Charact. 185 (2022) 111744.
- [62] M. Fu, Y. Yuan, X. Ma, X. Lin, A study of α variant selection in laser solid forming Ti-6Al-4V, J. Alloys Compd. 792 (2019) 1261–1266.
- [63] H. Beladi, Q. Chao, G.S. Rohrer, Variant selection and intervariant crystallographic planes distribution in martensite in a Ti–6Al–4V alloy, Acta Mater. 80 (2014) 478–489.
- [64] F. Niessen, A. Bhattacharyya, A.A. Gazder, E. V Pereloma, R.A. Lebensohn, Integrated multi-scale modeling of variant selection during stress-induced martensite formation in metastable β Ti-alloys, Acta Mater. (2022) 118342.
- [65] J. Zhang, X. Li, D. Xu, R. Yang, Recent progress in the simulation of microstructure evolution in titanium alloys, Prog. Nat. Sci. Mater. Int. 29 (2019) 295–304.
- [66] R. Shi, Y. Wang, Variant selection during α precipitation in Ti–6Al–4V under the influence of local stress A simulation study, Acta Mater. 61 (2013) 6006–6024.
- [67] D. Qiu, R. Shi, D. Zhang, W. Lu, Y. Wang, Variant selection by dislocations during α precipitation in α/β titanium alloys, Acta Mater. 88 (2015) 218–231.
- [68] J.S. Bowles, J.K. Mackenzie, The crystallography of martensite transformations I, Acta Metall. 2 (1954) 129–137.
- [69] J.K. Mackenzie, J.S. Bowles, The crystallography of martensite transformations—IV body-centred cubic to orthorhombic transformations, Acta Metall. 5 (1957) 137–149.
- [70] M.S. Wechsler, On the theory of martensitic transformations. The generalized lattice invariant shear and the degeneracy of solutions for the cubic to tetragonal transformation, Acta Metall. 7 (1959) 793–802.
- [71] Z. Nishiyama, M.E. Fine, M. Meshii, C.M. Wayman, S. Sato, E.S.& T. (Firm), Martensitic Transformation, Academic Press, 1978.
- [72] W. Pitsch, A. Schrader, Die Ausscheidungsform des ε-Karbids im Ferrit und im Martensit beim Anlassen, Arch. Für Das Eisenhüttenwes. 29 (1958) 715–721.